Superior Room Temperature Compressive Plasticity of Submicron Beta-Phase Gallium Oxide Single Crystals

Yueqin Wu, Qijian Rao, James P. Best,* Dekui Mu, Xipeng Xu, and Han Huang*

Bulk-scale ($\bar{2}$01)-oriented monoclinic beta-phase gallium oxide (β-Ga$_2$O$_3$) single crystals are brittle and fracture at low compressive strains. Here, it is reported that submicron β-Ga$_2$O$_3$ pillars exhibit an exceptional room temperature plastic strain of up to ≈22% under compression. Deformation is observed in transition from brittle to superior plasticity with reduction of pillar size. The critical diameter for the brittle to ductile transition is ≈800 nm, attributed to the initiation of dislocation slip on the primary (400) slip planes. Below 500 nm, a second transition is reported to superior plastic deformation, achieved through the activation of secondary mechanisms due to both deconfinement and low crystalline symmetry of β-Ga$_2$O$_3$, differentiating this finding from size-effected plasticity of other brittle materials where plasticity is attributed to dislocation slip on primary slip planes. Molecular dynamics simulation supports the proposed mechanism of pillar deconfinement where plastic deformation in larger pillars is solely dominated by planar defects on (400) slip planes, while secondary defects are induced for sufficiently small pillars. No plasticity is observed for equally dimensioned pillars tested on a (010)-oriented surface, highlighting the importance of presenting crystallography on submicron plasticity in this material.

1. Introduction

Single crystalline beta-phase gallium oxide (β-Ga$_2$O$_3$) is a promising transparent oxide semiconductor with bandgap

Y. Wu, Q. Rao, D. Mu, X. Xu
Institute of Manufacturing Engineering
Huaqiao University
Xiamen, Fujian 361021, China
Y. Wu, H. Huang
School of Mechanical and Mining Engineering
The University of Queensland
St Lucia, QLD 4072, Australia
E-mail: han.huang@uq.edu.au
J. P. Best
Max-Planck-Institut für Eisenforschung GmbH
Max-Planck-Str. 1, 40237 Düsseldorf, Germany
E-mail: j.best@mpie.de

The ORCID identification number(s) for the author(s) of this article can be found under https://doi.org/10.1002/adfm.202207960.

4.7–4.9 eV,[1,2] larger than SiC and GaN, also branded as a third-generation semiconductor with extensive applications in optoelectronic devices,[3,4] power electronics,[5,6] and gas sensors.[7] β-Ga$_2$O$_3$ single crystals have a monoclinic structure as shown schematically in **Figure 1a** and can be fabricated via melt-growth,[8–10] a cost-effective approach for mass production.[11] Like most inorganic single crystals,[12–15] it is intrinsically brittle and microscale specimens fracture at a relatively low compressive strain of 3.8% at room temperature.[16] Its brittle nature has brought great challenges for shaping raw crystals into high quality and precision substrates required for electronic and optical applications.[17] The development of a cost-effective machining technology necessitates a comprehensive understanding of deformation of the crystal; in particular the plasticity induced by microcontact associated with shaping.[18] Improved plastic deformability, avoiding catastrophic failure due to shock impact, is also of great importance for the application of inorganic semiconductors such as β-Ga$_2$O$_3$, especially in flexible electronic devices.

Plasticity in brittle inorganic semiconductors such as Si can often be induced through deformation at elevated temperatures.[19] Further, high temperature superplasticity has been demonstrated for fine-grained Si-based ceramics.[20–22] Only recently has progress been made in observing significant room temperature plasticity in bulk single crystals, reported for a range of semiconductors.[23–26] Deformation of brittle solids may also transit from brittle to ductile during room temperature indenting/scratching/cutting once the characteristic contact dimension is reduced below a critical value.[27,28] Size-effected plasticity has been recently reported from micropillar compression of a range of brittle materials, such as Si,[29–31] GaAs,[32] GaN,[15,33] MgO,[34] ZrB$_2$,[35] AlN,[36] and perovskite oxides.[37] In those cases, plastic deformation generally proceeds through strain bursts indicative of prevalent crystallographic slip. Further increasing the applied strain generally leads to fracture either along the primary slip plane, or at the intersection of two primary slip systems operating in the opposite direction.[38] Additional examples are summarized elsewhere.[39]

In this work, a high degree of size-activated room temperature plasticity for single crystal β-Ga$_2$O$_3$ was achieved through delocalization of slip from the primary slip plane (through the

**ADVANCED
SCIENCE NEWS**
www.advancedsciencenews.com

**ADVANCED
FUNCTIONAL
MATERIALS**
www.afm-journal.de

Figure 1. Schematic illustrations of (a) unit cell structure of β-Ga$_2$O$_3$ and (b) pillar compression testing. Post-mortem SEM images of compressed single crystalline β-Ga$_2$O$_3$ pillars with diameters of (c1) 2 µm, (d1) 685 nm, and (e1) 490 nm (taken at tilt angle of 52° and along the same crystalline direction), inset in (e1) is obtained after rotating the pillar axis by 90°; (c2), (d2), and (e2) the respective stress–strain curves obtained from the compression tests, pink crosses in (c2) and (d2) and pink arrow in (e2) indicate fracture initiation.

activation of secondary mechanisms) using uniaxial compression testing of submicron pillars. A commercially available ($\overline{2}$01)-oriented single crystalline β-Ga$_2$O$_3$ substrate with atomically smooth surface was used. A large plastic strain of up to ≈22% was observed for pillars with diameter <500 nm, where dominant dislocation slip along the primary slip plane was negated, differentiating our finding from size-effected plasticity of other brittle materials. An understanding of the deformation mechanisms promoting superior plasticity in β-Ga$_2$O$_3$ was achieved through a comprehensive analysis of deformed pillars using transmission electron microscopy (TEM), supported by molecular dynamics (MD) simulations.

2. Results and Discussion

2.1. Deformation with Reduction of Micropillar Diameter

Figure 1c–e shows scanning electron microscope (SEM) post-mortem images of representative single crystal β-Ga$_2$O$_3$ pillars 2000, 685 and 490 nm in diameter, respectively, together with corresponding stress-strain curves. All pillars were compressed to fracture and different fracture behaviors were evidenced for pillars with varying diameters.

For diameters at the micron scale (i.e., from ≈1 µm), pillars failed in a brittle manner at ca. 5% engineering strain, where fracture proceeded along the reported and presumed (200) primary slip plane that is preferential for fracture (Figure 1c1).[16] It must be noted that electron diffraction-based analyses of crystal defects cannot discriminate between (400) and (200), which are not equivalent in the monoclinic structure of β-Ga$_2$O$_3$. As the diameter was reduced to the submicron scale (i.e., 685 nm in Figure 1d1), the pillar underwent plastic deformation as reflected by the stress-strain curve (Figure 1d2) with failure at a higher strain of ≈15%. Multiple large discontinuities cor-

responding to slip events were observed before the occurrence of fracture as indicated by the pink cross in Figure 1d2, while fracture also occured along the (200) lattice plane as marked by the arrow in Figure 1d1. With further reduction of the pillar size to 490 nm (Figure 1e1), a greater plastic strain without obvious discontinuities was achieved prior to fracture (Figure 1e2). While the previous two examples showed fracture dominating along presumed (200) planes, for the smallest pillar dimensions some noticeable variation was observed (inset in Figure 1e1). The occurrence of the fracture event corresponds to the stress drop at 19% strain (indicated by the pink arrow on the stress-strain curve of Figure 1e2). As such, pillars with diameter <500 nm experience pure plastic deformation to high compressive strains, further evidenced through results of six micropillars <500 nm where compression was halted at an engineering strain of ≈15–20% and then unloaded; post-mortem imaging showed no evidence of fracture (see Figure 5). Detailed deformation mechanisms for pillars of varying diameters are unveiled in the following sections.

In total, over 30 pillars of diameters ranging from 400 nm to 2 µm (aspect ratio 2–2.5) were compressed until fracture. Results of fracture strain versus diameter are displayed in **Figure 2**a, while a full results list for the compressed pillars is provided in the Supporting Information (Table S3). With decreasing pillar diameter, the observed failure behavior can be classified into three distinct zones displaying the characteristics presented in Figure 1: brittle fracture along the primary slip plane; slip along the primary slip plane then fracture; superior plasticity then fracture. Superior plasticity is here defined by the presence of deformation characteristics that are not dominated by events along the primary slip plane. A sharp transition is observed in Figure 2a from the brittle fracture of larger pillars to a more graceful compressive failure to strains of ≈22%. The pillar diameter for the observable brittle-to-ductile transition

**ADVANCED
SCIENCE NEWS**

www.advancedsciencenews.com

**ADVANCED
FUNCTIONAL
MATERIALS**

www.afm-journal.de
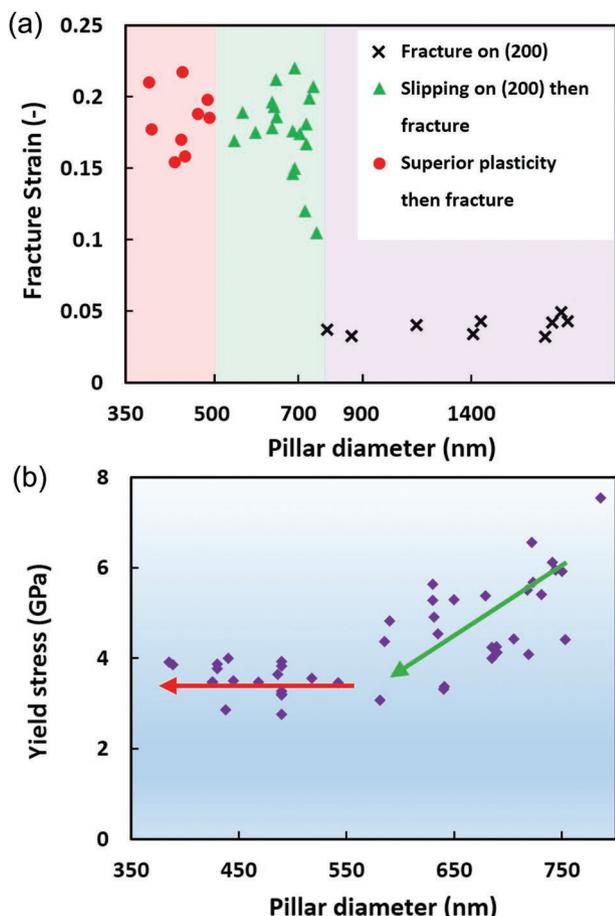
Figure 2. (a) Fracture strain plotted against pillar diameter. Three distinct deformation zones are highlighted, namely: fracture on (200); slip on (200) then fracture; superior plasticity then fracture. The *x*-axis is presented on a logarithmic scale. Fracture strains were obtained for 37 pillars. (b) Yield stress for pillars in the range of 400 to 800 nm diameter where plastic deformation was apparent. Yield stresses were obtained for 43 pillars with diameters smaller than 800 nm, including pillars unloaded prior to fracture.

(BDT) is ≈800 nm, while superior plasticity occurred in pillars with diameter <≈500 nm.

The yield stress is found to first decrease with reducing pillar diameter and then plateaus at pillar diameters lower than ≈550 nm (Figure 2b), while fracture stress remains relatively constant over the same size range (Figure S1, Supporting Information). This phenomenon might be rationalized as that below a certain transition point (≈550 nm in this case) confinement is sufficiently reduced to allow for initial activation of a secondary plasticity mechanism whose activation stress is constant. Only pillars that show plastic deformation are included in the plot in Figure 2b and Figure S1 (Supporting Information). The continuous decrease for larger micropillars to this plateau may therefore be due to continuously reducing confinement effects frustrating the activation of this secondary system. While the critical resolved shear stress (CRSS) to activate dislocations on specific slip systems is constant, a breakdown of Schmid's law is here expected,[40] allowing activation other plasticity systems (Table S2, Supporting Information) with potentially lower CRSS

operating before the primary (400) system. The observation of constant fracture stress ranging from 5 to 8 GPa with varying pillar diameter is not linked to the theoretical strength, based on MD simulation of compression perpendicular to ($\bar{2}$01) for β-Ga$_2$O$_3$ (Figure S7, Supporting Information), however could be linked to the onset of defect nucleation. This view is enhanced by the observation that significant numbers of pre-existing dislocations are not expected in the micropillars due to the low dislocation density of the β-Ga$_2$O$_3$ crystal (10^3–10^5 cm^{-2}),[41] with little difference in initial defect state between pillars of different sizes. However, it is also noted that the fracture modes between pillars of different diameters vary, and direct inferences are not straight-forward to establish.

Pillars were additionally fabricated and tested on a (010)-oriented β-Ga$_2$O$_3$ crystal, and consistently showed brittle deformation (failure in the linear elastic regime), including for pillars <500 nm diameter tested over two decades of strain rate (5–500 nm s^{-1}) (**Figure 3**). For (010)-oriented β-Ga$_2$O$_3$ crystals, the (200) and (400) planes are oriented perpendicular to the pillar top surface with minimized resolved shear stress during compression (Figure 3a). Therefore, there is a high barrier to activate plastic deformation on those planes and the material fails in a brittle manner, explaining the absence of plasticity compared to ($\bar{2}$01)-oriented pillars. Such orientation effects may be important for machining applications where more complex stress fields are encountered,[42] opposed to the uniaxial stress states studied here. Anisotropic phenomena were also observed in the compression of nanodeconfined GaN pillars; room-temperature plasticity was evidenced during M-direction compression while a quasi-brittle response was produced along the C direction.[33]
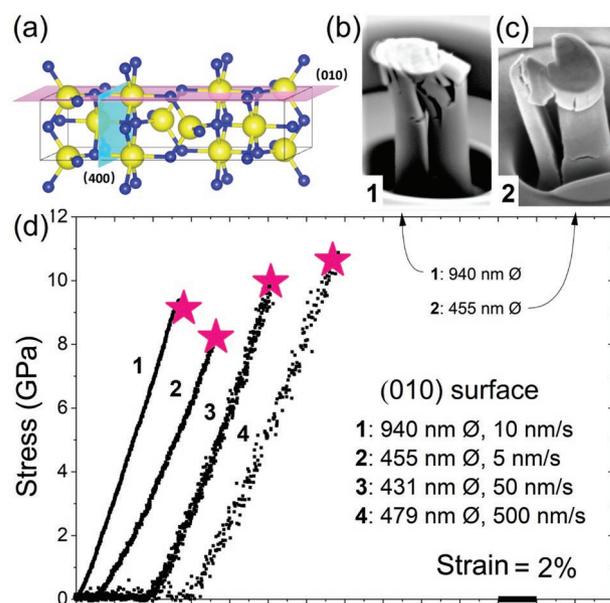
Figure 3. Uniaxial compression of (010)-oriented micropillars. (a) β-Ga$_2$O$_3$ unit cell with the (010) surface orthogonal to the compression direction. (b) and (c) show postmortem SEM images of compressed micropillars with diameters 940 and 455 nm, respectively. (d) Representative engineering stress-strain curves highlighting fracture event (pink star). Various pillar diameters and strain rates were tested. For all tested samples a brittle fracture response was observed with no plasticity. Data has been artificially shifted on the *x*-axis for clarity.

**ADVANCED
SCIENCE NEWS**

www.advancedsciencenews.com

**ADVANCED
FUNCTIONAL
MATERIALS**

www.afm-journal.de

2.2. Deformation Mechanisms for Varying Pillar Diameters

2.2.1. Fracture Along Primary Slip Plane (Pillar Diameter >800 nm)

The deformation characteristics of single crystalline β-Ga$_2$O$_3$ pillars at the micron scale were investigated previously.[16] The deformation was dominated by brittle fracture along the presumed (200) plane with an average fracture stress of 7.25 ± 1.1 GPa and failure strain of 3.8 ± 0.57%.[16] The observations obtained in this work for pillars with a diameter >800 nm are consistent with this.

2.2.2. Plasticity Along Primary Slip Plane then Fracture (Pillar Diameter 500–800 nm)

To understand plastic deformation for pillars in this size range, a 650 nm diameter pillar was compressed to a maximum strain of ≈10% and preceding fracture (**Figure 4**). The volume of each fabricated pillar has a statistically negligible chance of containing a dislocation due to an extremely low pre-existing dislocation density in the crystal (10^3–10^5 cm^{-2}).[41] However, a thin surface defect layer <10 nm in thickness is induced during pillar fabrication using focused ion beam (FIB) (more details provided in Supporting Information E).[16] Any defects within the pillar volume are thus induced by compression. Deformation was examined using TEM where Figure 4c shows the cross-sectional bright field (BF) TEM image obtained along a [010] zone axis, confirming slip on (200). The imaged slip step geometry correlates well to the strain burst observable in the load-displacement curve (inset in Figure 4d, further details in Supporting Information A1). Additional representative pillars of diameter 650–875 nm are presented in Figure S2a–c (Supporting Information), where surface deformation features were less apparent and the relative magnitudes of discontinuities in stress-strain curves decreased for smaller pillars (Figure S2d–f,
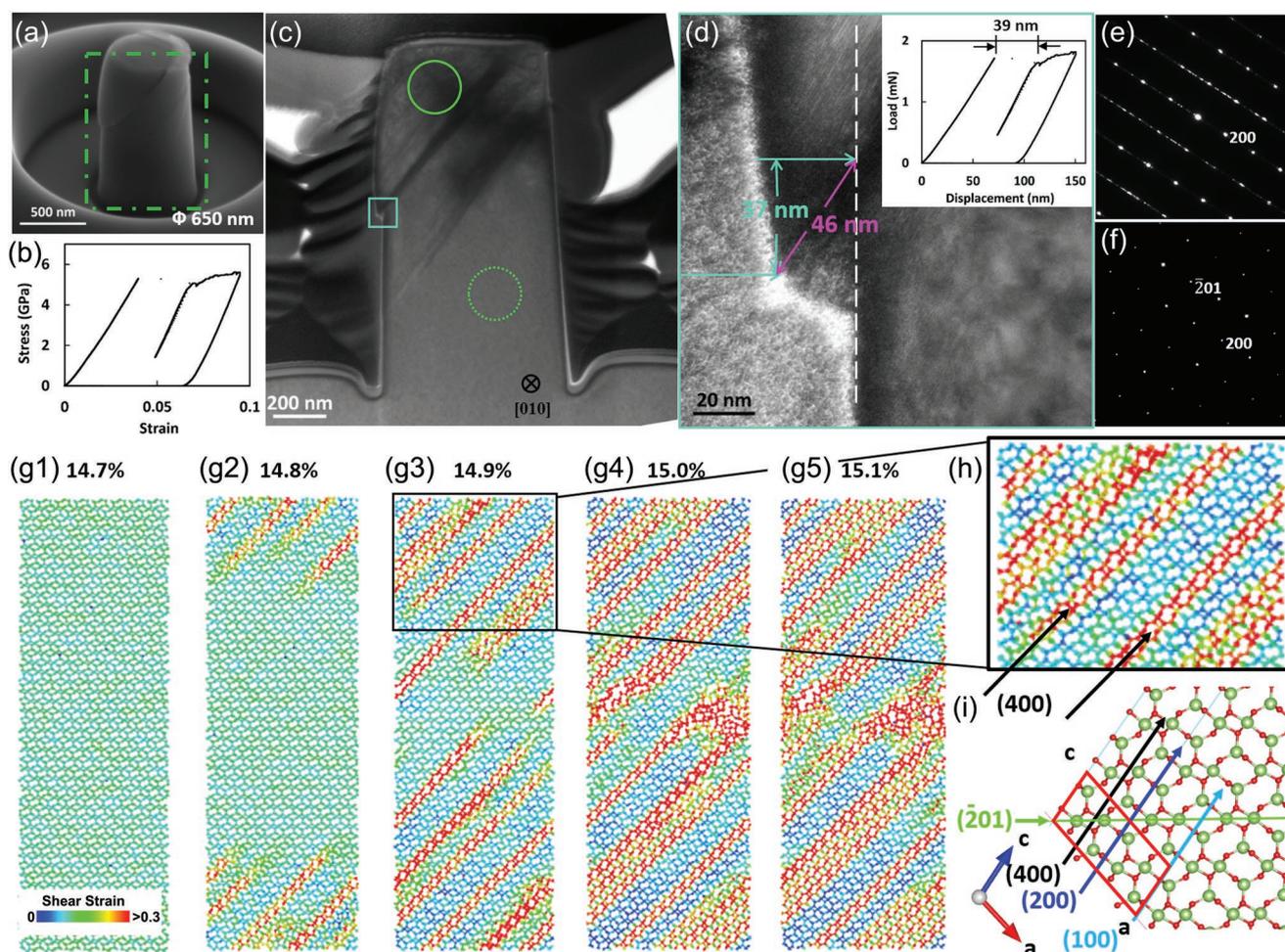
Figure 4. (a) SEM image of 650 nm pillar after compression at a maximum strain of ≈10% (taken at tilt angle of 52°) and (b) corresponding stress-strain curve. (c) Cross-sectional BF TEM image of the compressed pillar observed along the [010] zone axis. (d) High magnification TEM image obtained from the boxed area in (c) for slip step analysis and corresponding load-displacement curve (inset). (e) and (f) are SAED patterns acquired from the areas marked by the solid and dashed circles in (c), respectively. The atomic models for MD simulation at compressive strains of (g1) 14.7%, (g2) 14.8%, (g3) 14.9%, (g4) 15.0%, and (g5) 15.1%, observed in [010]. (h) Magnified image of atoms taken from the boxed area in (g3). (i) Atomic model of the undeformed β-Ga$_2$O$_3$ crystal structure where the red parallelogram represents a unit cell. Increased deformation observed towards the top of the pillar in experiments caused by 3–5° pillar taper and resulting stress enhancement at the top surface.

**ADVANCED
SCIENCE NEWS**

www.advancedsciencenews.com

**ADVANCED
FUNCTIONAL
MATERIALS**

www.afm-journal.de

Supporting Information). The existence of diffraction spots with streaking along 200 (Figure 4e) suggests that high density stacking faults were generated on the presumed (200) planes, consistent with previous observations.[43] Stacking faults were also reported for ground single crystalline β-Ga$_2$O$_3$.[44,45] It is thus inferred that stacking faults were first induced on the top surface during compression and started to slip along (200) planes once the resolved shear stresses were sufficiently high. Such a deformation mechanism is similar to those of deformed semiconductors that exhibit a certain degree of plasticity, such as Si,[29,30] GaAs,[32] AlN,[36] and GaN.[15]

The deformation of single crystal β-Ga$_2$O$_3$ under uniaxial compression was further investigated by MD simulation. Pillars in the 500–800 nm diameter size range were simulated using periodic boundary conditions (PBC), where details on the MD simulation and analysis are provided in Supporting Information F2. As shown in Figure 4g1–5, the simulation confirmed the occurrence of planar defects once the strain exceeded 14.7% and the defects extended with the increased strain, detailed in Supporting Information B. The planar defects were identified on (200) planes by TEM, however, MD simulation more precisely demonstrates that the planar defects were preferentially nucleated on (400) planes by matching the atomic structure of the defect planes indicated by the black arrows in Figure 4h and the crystal structure model of undeformed β-Ga$_2$O$_3$ in Figure 4i. It should be again noted that conventional TEM observation cannot distinguish between the parallel (400) and (200) planes. This shows the capability of MD simulation for in-depth understanding of crystal structure evolution at atomic scale.

Combining the SEM/TEM observations and MD simulation results, it is concluded that for pillars of 500–800 nm in diameter planar defects on (400) planes are first initiated, followed by multiple slip events with increased compressive strain. Pillars fracture along the (400) plane once the stress is sufficiently high.

2.2.3. Superior Plasticity then Fracture (Pillar Diameter <500 nm)

Similar to that presented above, a 490 nm pillar was compressed to a maximum strain of ≈20% and unloaded prior to fracture to understand the deformation of pillars in this size range. As seen in **Figure 5**a, the pillar exhibits a more complex deformation character, and no cracks are observed; also reflected in the relatively smooth stress-strain curve (Figure 5b), where no large discontinuity is evidenced. Even though compressed to a strain of nearly 20% the pillar shows a continuous barreled surface without observable slip steps (Figure 5c), consistent with post-mortem SEM imaging, indicating that a dominating primary slip on (400) may be avoided for sufficiently small pillars. Due to a small taper (3–5°) produced during pillar fabrication, initial compression stresses are concentrated towards the pillar top surface. As such, it is presumed for smaller pillar diameters that material in the upper pillar volume deforms laterally without dominant slip on (400) during compression, accommodating significant strain. This finding is novel for eminently brittle semiconductor materials at room temperature, and as such the mechanism needs to be unveiled.

Both selected-area electron diffraction (SAED) pattern (Figure 5d) and high resolution TEM image (Figure 5f)

acquired from the severely deformed area in the top part of the pillar show that the lattice arrangement was severely distorted (detailed analysis in Supporting Information A2). The atomic bonding structure in this region appeared to be altered due to the compressive strain, which was not observed in the larger pillars where only planar defects were observed. Pillars <500 nm eventually failed when the strain was sufficiently large. Combining the SEM and TEM images presented in Figure S4 (Supporting Information), the deformation and subsequent fracture behavior of the pillars <500 nm varied considerably from those >800 nm in which fracture occurred exclusively along the primary (400) slip plane.

MD simulation was also used to investigate the deformation of pillars in the size range exhibiting superior plastic characteristics. Cylindrical models with varying diameters were employed, whose detailed simulation analysis can be found in Supporting Information F2. Typical MD results for a cylindrical model with diameter of 8 nm and aspect ratio of 2 are presented in Figure 5g1–8 at varying strain levels. A planar defect on a (400) plane was initiated from the top corner of the pillar when the strain exceeded 9.25% (Figure 5g2), and extended until traversing the whole pillar breadth (Figure 5g4). The defects shown at the top left corner of Figure 5g5 were additionally induced, which penetrated deeper into the pillar and encountered a planar defect on the (400) plane formed previously with the strain increased to 11% (Figure 5g6). Further compression led to a more severe deformation in the top part of the pillar, whose crystal structure became amorphous in the vicinity of the defects as seen in Figure 5g8. The final pillar exhibits a barreling shape indicative of delocalized plastic deformation, consistent with experimental observations. Previous studies support amorphization in complex crystal structures, e.g. amorphous shear bands were found both experimentally and in simulations for intermetallic SmCo$_5$,[46,47] or SiC where planar stacking faults are reported to serve as precursors for amorphization.[48]

2.3. Deconfinement Effects During Pillar Compression

To elucidate how size-effects govern deformation, various pillar diameters were studied using MD simulations with cylindrical models. Representative results are shown in Figure 5h. When the pillar diameter is relatively large, i.e. 10 nm, planar defects on (400) plane are first initiated (Figure 5h3'); broadly equivalent to the MD results using periodic boundary conditions (Figures 4g and 5h4). Thus the 10 nm model can bridge the MD models for small pillars and those using periodic boundary conditions for large pillars. Detailed structure evolution for 10 nm model can be found in Supporting Information C1 and Figure S5 (Supporting Information).

When the pillar diameter is reduced to 6 nm, the occurrence of planar defects on (400) planes is not observed, instead severe deformation along approximate (002) lattice planes is induced (Figure 5h1' and Figure S6, Supporting Information). The lateral atomic confinement from neighboring atoms in the 6 nm model is reduced compared to that of 10 nm model, leading to varying stress distributions. Consequently the deformation patterns also vary, and the absence of observable planar defects on (400) is therefore likely due to a deconfinement effect in the smaller pillar.[33,49,50] An increased level of surface defects is also
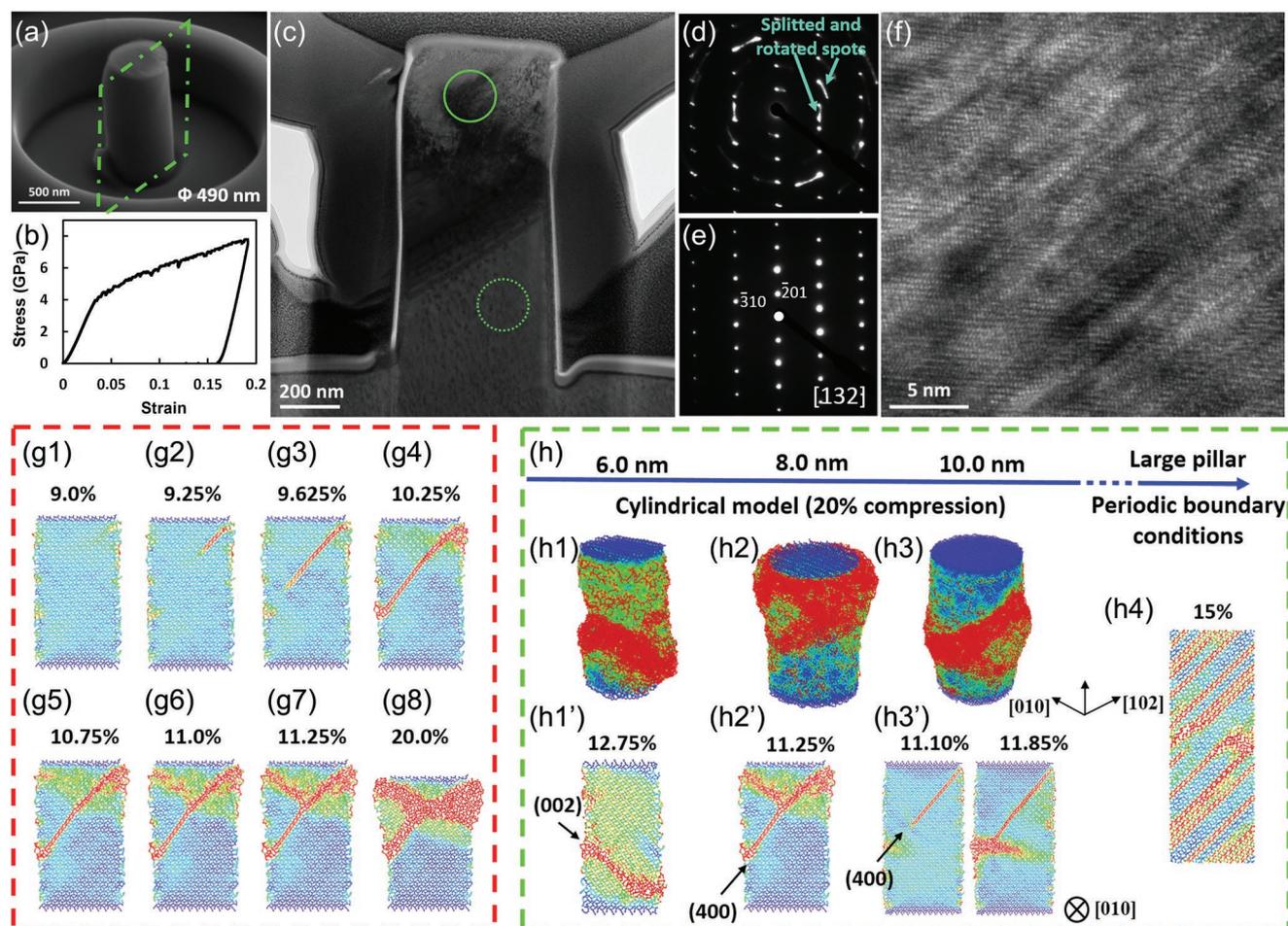
Figure 5. (a) SEM image of 490 nm diameter pillar after compression to a maximum strain of ≈20% (taken at tilt angle of 52°) and (b) corresponding stress-strain curve. (c) Cross-sectional BF TEM image of the compressed β-Ga$_2$O$_3$ pillar along its [132] zone axis. (d) and (e) are SAED patterns acquired from the areas marked by the solid and dashed circles in (c), respectively. (f) High resolution TEM image obtained from the severely deformed area at the top part of the pillar. (g1) to (g8) MD simulation results using a cylindrical model for an 8 nm β-Ga$_2$O$_3$ pillar at increasing strains, for a [010] observation direction. (h) Summary of size-effect on the MD simulation. MD simulation results for pillars with diameter of (h1) 6 nm, (h2) 8 nm, and (h3) 10 nm using cylindrical models and (h4) using model with periodic boundary conditions. (h1'–h3') are cross-sectional view of the pillars when the representative planar defects were initiated. Please note diameters here denote the diameter of the pillars prior to compression with aspect ratio 2. The image sizes do not scale with the pillar size.

generated during compression (Figure S6, Supporting Information), which may affect the deformation response. Stress-strain curves obtained from the MD simulations are shown in Figure S7a (Supporting Information) and a detailed analysis is provided in Supporting Information C2. The elastic strain limit decreases with the reduction of pillar size, together with yield stress (Figure S7b, Supporting Information), consistent with the experimental results in Figure 2b, and further confirming the existence of deconfinement effects.

The 8 nm model (Figure 5h2') sits between the above two situations, where a planar defect on (400) plane is first initiated followed by severe deformation on the approximate (002) lattice plane. Experimentally, planar defects on (400) planes also exist along with other defects and distortions for pillar diameters under the critical size (≈500 nm) for superior plasticity. This is additionally reflected by TEM and SAED characterizations of a 490 nm diameter pillar compressed to a strain of 6%, detailed in Supporting Information D and Figure S8 (Supporting Information). Because the size of MD models is far smaller than that in experiment, MD simulation is not expected to fully interpret the experimental results. Nevertheless, the size effect from MD is consistent with experiments; defects other than those on (400) planes initiate for pillars <500 nm diameter during uniaxial compression and <8 nm in MD simulation. This is rational considering the monoclinic crystal structure of β-Ga$_2$O$_3$ with low space symmetry; it possesses a large number of possible slip systems along close packed crystal planes beside (400), i.e., ($\bar{2}$01), (101), ($\bar{3}$10), and ($\bar{3}\bar{1}$0), as verified using synchrotron radiation X-ray topography.[51,52] Activation of these slip systems appear to not be energetically favorable for large crystal volumes, however activation may occur when deconfinement and the role of surface defects becomes significant in sufficiently small pillars with reduced lateral constraint. The entanglement of crystal defects on multiple lattice planes may lead to significant frustration of slip on (400) planar defects leading to a delocalization of plasticity. The

**ADVANCED
SCIENCE NEWS**

www.advancedsciencenews.com

**ADVANCED
FUNCTIONAL
MATERIALS**

www.afm-journal.de

determination of specific activated slip systems or dislocations analyses were however not possible using conventional TEM analysis or MD simulation. Due to the interaction of defects on varied lattice planes and crystal directions as explained in Supporting Information D and Figure S8 (Supporting Information) a direct analysis of dislocation motion from conventional TEM observation was not attainable, while the current dislocation extraction algorithm was not able to analyze the MD simulation results for this material with monoclinic structure and low crystalline symmetry. Theoretically, future work harnessing a more powerful dislocation extraction algorithm, or an in situ TEM examination of compression might provide approaches to fully disclose the specific dislocation activities in pillars with large plasticity. To provide some insight, Peierls stresses and Schmid factors considering a compression axis perpendicular to $(\bar{2}01)$ were calculated as detailed in Supporting Information F3 and are presented in Table S2 (Supporting Information). It can be inferred that other slip system(s) other than the primary (400) slip, i.e., (002)<100>, $(\bar{3}10)$<001>, or $(\bar{3}10)$<001>, are likely candidates to activate for the small pillars due to deconfinement and a breakdown of Schmid's law. However, that such mechanisms are not active in the (010)-oriented crystals hints that the initial activation of stacking faults on (400) planes may also play a significant role, as has been reported for SiC.[48] The superior plasticity is realized by slightly sacrificing its elastic limit through a reduced yield strength in the activation of secondary systems. This may be an acceptable trade-off in applications where increased plastic deformation is valued over high fracture strengths, as for micromachining.

3. Conclusions

In summary, transitions from brittle to plastic (<≈800 nm), and finally to superior plastic (<≈500 nm), deformation of $(\bar{2}01)$-oriented single crystalline β-Ga_2O_3 upon reduction of micropillar diameter was observed using uniaxial compression at room temperature. The presenting crystallographic orientation of the micropillars was found to be crucial for observation of plasticity at small scales. Slip on the primary (400) plane was seen to dominate till 500 nm diameter, whereafter superior plasticity and reduced yield strength through activation of secondary mechanisms was achieved due to lateral deconfinement and the low symmetry of β-Ga_2O_3. The ultra-high plasticity of this eminently brittle material is desirable for applications at nano- to micrometer scales. The observed mechanisms of superior plasticity are of significance, and open up new opportunities to study and leverage the exceptional mechanical properties of semiconductors with low symmetry crystal structures.

4. Experimental Section

Micropillar Fabrication: Commercially available $(\bar{2}01)$-oriented single crystalline β-Ga_2O_3 substrate with atomically smooth surface was used. Micropillars of diameters ranging from 400 nm to 2 μm (measured at the middle of the pillars) were fabricated using FEI Scios FIB–Dual Beam SEM system. The detailed pillar fabrication process can be found elsewhere.[16] The aspect ratio (length/diameter) of the pillars

was controlled in the range of from 2 to 2.5 to avoid bulking during compression testing. All the SEM images of the compressed pillars were obtained using the same tilt angle of 52° and sample rotation angle unless specified. For micropillars testing on the (010) surface a separate single crystal was used, and pillars milled using a Zeiss Auriga dual-beam FIB-SEM with equivalent milling conditions.

Compression Testing: Uniaxial compression testing of the $(\bar{2}01)$-oriented pillar was conducted on a Hysitron TriboIndenter system. A flat-end diamond tip that has a circular cross section of 10 μm in diameter was used as the press punch. Displacement controlled mode was used during compression testing and the displacement rate was set to 5 nm s⁻¹. The minor strain rate difference caused by using constant displacement speed for varying pillar diameters is not expected to affect the deformation of compressed $(\bar{2}01)$-oriented pillars. The load-displacement curve was recorded, which was used to derive the stress–strain curve. For micropillars testing on the (010) surface an Alemnis ASA (Alemnis AG, Switzerland) was used with nominal 2 μm diameter diamond flat-punch counter-body (Synton-MDP AG, Switzerland). Testing was performed in situ within a Zeiss Gemini SEM. The displacement rate was controlled between 5 and 500 nm s⁻¹ to test any strain-rate influences for the smaller pillar diameters.

TEM Characterization: The cross-sectional TEM specimens of compressed β-Ga_2O_3 micropillars were prepared using a FIB lift-out technique.[53] A layer of platinum was deposited to protect the micropillar from damage during subsequent ion milling. Platinum was also used to fill the trench to avoid uneven milling. TEM lamellae were cut perpendicular to the zone axis of either [010] or [132], and through the centre of the compressed pillar. TEM examination was carried out on a Philips Tecnai F20 TEM, operating at 200 kV.

Statistical Analysis: In total, 37 pillars were compressed till fracture, consisting of: nine showing "fracture on (200)"; 19 for "slip on (200) then fracture"; nine for "superior plasticity then fracture." Yield stresses were obtained for 43 pillars with diameters smaller than 800 nm, including pillars unloaded prior to fracture.

Supporting Information

Supporting Information is available from the Wiley Online Library or from the author.

Conflict of Interest

The authors declare no conflict of interest.

Data Availability Statement

The data that support the findings of this study are available from the corresponding author upon reasonable request.

[1] H. H. Tippins, *Phys. Rev.* **1965**, *140*, A316.

[2] S. J. Pearton, J. Yang, P. H. CaryIV, F. Ren, J. Kim, M. J. Tadjer, M. A. Mastro, *Appl. Phys. Rev.* **2018**, *5*, 011301.

[3] S. I. Stepanov, V. I. Nikolaev, V. E. Bougrov, A. E. Romanov, *Rev. Adv. Mater. Sci.* **2016**, *44*, 63.

[4] M. M. Muhammed, M. Peres, Y. Yamashita, Y. Morishima, S. Sato, N. Franco, K. Lorenz, A. Kuramata, I. S. Roqan, *Appl. Phys. Lett.* **2014**, *105*, 042112.

[5] M. Higashiwaki, K. Sasaki, A. Kuramata, T. Masui, S. Yamakoshi, *Appl. Phys. Lett.* **2012**, *100*, 013504.

[6] M. A. Mastro, A. Kuramata, J. Calkins, J. Kim, F. Ren, S. J. Peartong, *ECS J. Solid State Sci. Technol.* **2017**, *6*, P356.

[7] M. Bartic, C.-I. Baban, H. Suzuki, M. Ogita, M. Isai, *J. Am. Ceram. Soc.* **2007**, *90*, 2879.

[8] Z. Galazka, R. Uecker, K. Irmscher, M. Albrecht, D. Klimm, M. Pietsch, M. Brützam, R. Bertram, S. Ganschow, R. Fornari, *Cryst. Res. Technol.* **2010**, *45*, 1229.

[9] V. I. Nikolaev, V. Maslov, S. I. Stepanov, A. I. Pechnikov, V. Krymov, I. P. Nikitina, L. I. Guzilova, V. E. Bougrov, A. E. Romanov, *J. Cryst. Growth* **2017**, *457*, 132.

[10] E. G. Villora, K. Shimamura, Y. Yoshikawa, K. Aoki, N. Ichinose, *J. Cryst. Growth* **2004**, *270*, 420.

[11] Gallium Oxide Trumps Traditional Wide Bandgap Semiconductors, https://compoundsemiconductor.net/article/89570/Gallium_oxide_trumps_traditional_wide_bandgap_semiconductors_, (accessed: September 2022).

[12] G. M. Cheng, Y. Zhang, T. H. Chang, Q. F. Liu, L. Chen, W. D. Lu, T. Zhu, Y. Zhu, *Nano Lett.* **2019**, *19*, 5327.

[13] J. Michler, K. Wasmer, S. Meier, F. Ostlund, K. Leifer, *Appl. Phys. Lett.* **2007**, *90*, 043123.

[14] X. L. Guo, Q. Guo, Z. Q. Li, G. L. Fan, D. B. Xiong, Y. S. Su, J. Zhang, Z. Q. Tan, C. P. Guo, D. Zhang, *Metall. Mater. Trans. A* **2018**, *49*, 439.

[15] S. F. Fan, X. C. Li, R. Fan, Y. Lu, *Nanoscale* **2020**, *12*, 23241.

[16] Y. Q. Wu, S. Gao, R. K. Kang, H. Huang, *J. Mater. Sci.* **2019**, *54*, 1958.

[17] D. B. Holt, B. G. Yacobi, *Extended Defects in Semiconductors : Electronic Properties, Device Effects and Structures*, Cambridge University Press, Cambridge, **2007**.

[18] H. Huang, X. L. Li, D. K. Mu, B. R. Lawn, *Int. J. Mach. Tools Manuf.* **2021**, *161*, 103675.

[19] P. B. Hirsch, S. G. Roberts, J. Samuels, *Proc. R. Soc. A* **1989**, *421*, 25.

[20] F. Wakai, Y. Kodama, S. Sakaguchi, N. Murayama, K. Izaki, K. Niihara, *Nature* **1990**, *344*, 421.

[21] Y. Shinoda, T. Nagano, H. Gu, F. Wakai, *J. Am. Ceram. Soc.* **1999**, *82*, 2916.

[22] R. Wananuruksawong, Y. Shinoda, T. Akatsu, F. Wakai, *Scr. Mater.* **2015**, *103*, 22.

[23] Y. Oshima, A. Nakamura, K. Matsunaga, *Science* **2018**, *360*, 772.

[24] X. Shi, H. Y. Chen, F. Hao, R. H. Liu, T. Wang, P. F. Qiu, U. Burkhardt, Y. Grin, L. D. Chen, *Nat. Mater.* **2018**, *17*, 421.

[25] T.-R. Wei, M. Jin, Y. Wang, H. Chen, Z. Gao, K. Zhao, P. Qiu, Z. Shan, J. Jiang, R. Li, L. Chen, J. He, X. Shi, *Science* **2020**, *369*, 542.

[26] H. Y. Chen, T. R. Wei, K. P. Zhao, P. F. Qiu, L. D. Chen, J. He, X. Shi, *InfoMat* **2021**, *3*, 22.

[27] B. R. Lawn, H. Huang, M. Lu, Ó. Borrero-López, Y. Zhang, *Acta Mater.* **2022**, *232*, 117921.

[28] H. Huang, B. R. Lawn, R. F. Cook, D. B. Marshall, *J. Am. Ceram. Soc.* **2020**, *103*, 6096.

[29] A. Merabet, M. Texier, C. Tromas, S. Brochard, L. Pizzagalli, L. Thilly, J. Rabier, A. Talneau, Y. M. Le Vaillant, O. Thomas, J. Godet, *Acta Mater.* **2018**, *161*, 54.

[30] F. Ostlund, K. Rzepiejewska-Malyska, K. Leifer, L. M. Hale, Y. Y. Tang, R. Ballarini, W. W. Gerberich, J. Michler, *Adv. Funct. Mater.* **2009**, *19*, 2439.

[31] M. Chen, L. Pethö, A. S. Sologubenko, H. Ma, J. Michler, R. Spolenak, J. M. Wheeler, *Nat. Commun.* **2020**, *11*, 2681.

[32] F. Ostlund, P. R. Howie, R. Ghisleni, S. Korte, K. Leifer, W. J. Clegg, J. Michler, *Philos. Mag.* **2011**, *91*, 1190.

[33] M. Fujikane, S. Nagao, D. Chrobak, T. Yokogawa, R. Nowak, *Nano Lett.* **2021**, *21*, 6425.

[34] S. Korte, M. Ritter, C. Jiao, P. A. Midgley, W. J. Clegg, *Acta Mater.* **2011**, *59*, 7241.

[35] T. Csanádi, P. Szommer, N. Q. Chinh, S. Grasso, J. Dusza, M. Reece, *J. Eur. Ceram. Soc.* **2016**, *36*, 389.

[36] J. J. Guo, K. Madhav Reddy, A. Hirata, T. Fujita, G. A. Gazonas, J. W. McCauley, M. W. Chen, *Acta Mater.* **2015**, *88*, 252.

[37] Y. Liu, X. Cui, R. Niu, S. Zhang, X. Liao, S. D. Moss, P. Finkel, M. Garbrecht, S. P. Ringer, J. M. Cairney, *Nat. Commun.* **2022**, *13*, 335.

[38] P. R. Howie, S. Korte, W. J. Clegg, *J. Mater. Res.* **2012**, *27*, 141.

[39] S. Korte-Kerzel, *MRS Commun.* **2017**, *7*, 109.

[40] K. S. Ng, A. H. W. Ngan, *Scr. Mater.* **2008**, *59*, 796.

[41] Y. Z. Yao, Y. Sugawara, Y. Ishikawa, *Jpn. J. Appl. Phys.* **2020**, *59*, 045502.

[42] Y. Q. Wang, X. L. Li, Y. Q. Wu, D. K. Mu, H. Huang, *Int. J. Mech. Sci.* **2021**, *204*, 106562.

[43] Y. Q. Wu, S. Gao, H. Huang, *Mater. Sci. Semicond. Process.* **2017**, *71*, 321.

[44] S. Gao, Y. Q. Wu, R. K. Kang, H. Huang, *Mater. Sci. Semicond. Process.* **2018**, *79*, 165.

[45] Y. Q. Wu, D. K. Mu, H. Huang, *Int. J. Extreme Manuf.* **2020**, *2*, 012006.

[46] H. B. Luo, H. W. Sheng, H. L. Zhang, F. Q. Wang, J. K. Fan, J. Du, J. P. Liu, I. Szlufarska, *Nat. Commun.* **2019**, *10*, 3587.

[47] H. B. Luo, H. L. Zhang, H. W. Sheng, J. P. Liu, I. Szlufarska, *Mater. Sci. Eng. A* **2020**, *785*, 139340.

[48] S. Zhao, R. Flanagan, E. N. Hahn, B. Kad, B. A. Remington, C. E. Wehrenberg, R. Cauble, K. More, M. A. Meyers, *Acta Mater.* **2018**, *158*, 206.

[49] D. Chrobak, N. I. Tymiak, A. R. Beaber, O. Ugurlu, W. W. Gerberich, R. J. N. N. Nowak, *Nat. Nanotechnol.* **2011**, *6*, 480.

[50] Y. He, L. Zhong, F. F. Fan, C. M. Wang, T. Zhu, S. X. Mao, *Nat. Nanotechnol.* **2016**, *11*, 866.

[51] H. Yamaguchi, A. Kuramata, T. Masui, *Superlattices Microstruct.* **2016**, *99*, 99.

[52] Y. Z. Yao, Y. Ishikawa, Y. Sugawara, *Jpn. J. Appl. Phys.* **2020**, *59*, 125501.

[53] R. M. Langford, A. K. Petford-Long, *J. Vac. Sci. Technol., A* **2001**, *19*, 2186.